Renewable and Sustainable Energy Reviews 26 (2013) 727–738

Contents lists available at SciVerse ScienceDirect

Renewable and Sustainable Energy Reviews

journal homepage: www.elsevier.com/locate/rser

Power flow control Methods for an ultracapacitor bidirectional converter in DC microgrids—A comparative study

O.A. Ahmed*, J.A.M. Bleijs

Department of Engineering, University of Leicester, University Road, Leicester LE1 7RH, UK

ARTICLE INFO

Article history:
Received 7 February 2013
Received in revised form
31 May 2013
Accepted 16 June 2013
Available online 12 July 2013

Keywords:
Bidirectional converter
Phase-shift modulation
Ultracapacitor
Microgrid

ABSTRACT

Distributed generation in the form of DC microgrids has recently attracted increasing research interest. For integrating renewable energy resources and energy storage devices, such as an ultracapacitor, to the DC bus of a DC microgrid and sustain the charging and discharging states of the ultracapacitor, a bidirectional DC–DC converter is required. For the fast dynamic response of the ultracapacitor, bidirectional voltage-fed topology is preferred. But for a wide input voltage variation of the ultracapacitor, this topology exhibits a higher circulating power flow and higher conduction losses as a consequence. In this paper a comprehensive overview on several modulation methods that employed to control the power flow of the bidirectional voltage-fed DC–DC converter for the ultracapacitor applications are presented. A detailed analysis of the bidirectional converter exploring the impact of the circulating power flow interval is developed in this study. Analytical methods have been applied to establish alternative modulation methods for the bidirectional converter to improve its performance and efficiency.

Contents

1. Introduction . . . 727
2. Working principle of BDC . . . 729
3. Conventional phase-shift modulation scheme . . . 730
   3.1. SSW analysis . . . 731
   3.2. RMS analysis . . . 732
   3.3. Circulating power flow (CPF) analysis . . . 733
4. Alternative phase-shift modulation schemes . . . 733
   4.1. Triangular current modulation . . . 734
   4.2. Modified triangular current modulation . . . 735
   4.3. Hybrid modulation schemes . . . 736
      4.3.1. PTRM–CPC hybrid modulation . . . 736
      4.3.2. TRM–TZM hybrid modulation . . . 736
      4.3.3. TRM–TZM–CPC combination . . . 737
      4.3.4. Composite dual PWM scheme . . . 737
   4.4. Voltage-balance modulation scheme . . . 737
5. Conclusions . . . 737
References . . . 738

1. Introduction

Traditional power systems are facing a number of problems such as low energy efficiency, environmental pollution, drastic increases of the fossil fuel prices, and gradual depletion of fossil fuel resources. These problems have led to the development of a

* Corresponding author. Tel.: +9647715214563.
E-mail addresses: oa49@alumni.le.ac.uk, oday_ali@uotechnology.edu.iq (O.A. Ahmed).

1364-0321/$ - see front matter © 2013 Elsevier Ltd. All rights reserved.
http://dx.doi.org/10.1016/j.rser.2013.06.021

new concept for power generation so as to generate electricity locally by utilising small non-conventional and renewable energy sources such as microturbines, back-up diesel generators, wind turbines, solar photovoltaic cells, and fuel cells [1]. The increase in distributed generation penetration depth and the presence of multiple distributed generation units in electrical network within a certain local area in close proximity to one another have brought about the concept of the "microgrid" [2].

Microgrid architectures for integrating renewable energy resources can be classified into AC or DC bus interconnections. Recently, DC microgrid have shown promising features such as improving the grid efficiency and the power quality in addition to increase the penetration of the renewable energy sources to the microgrid bus and elimination of DC–AC power conversion stage required in AC microgrid for the renewable sources and loads. Fig. 1 shows the basic configuration of DC microgrid. As can be seen that the DC microgrid may comprise both dispatchable power generators such as a fuel cell (FC), back-up diesel generator or micro (gas) turbines, and non-dispatchable generators, such as solar photovoltaic and wind turbines, and energy storage, in the form of ultracapacitors (UC) or batteries. In the DC microgrid configuration, all of the above generators and storage units are connected to the DC bus-bar.

In practice an energy storage unit, such as UC, is usually considered an essential requirement for a microgrid to allow instantaneous power balancing of renewable energy resources and loads when the microgrid is disconnected from the utility grid (islanding or autonomous) and to ensure uninterrupted supply to priority loads. In addition, the energy storage devices operate in the microgrid system to store surplus energy.

Most of the storage devices such as batteries and ultracapacitors produce a DC voltage, thus a bidirectional DC–DC converter (BDC) is utilised to interface them to the DC bus of a DC microgrid and to manage the power flow between the renewable sources, the UC storage and the load. Both voltage-fed and current-fed topologies can be used as a BDC to fulfil the requirements for

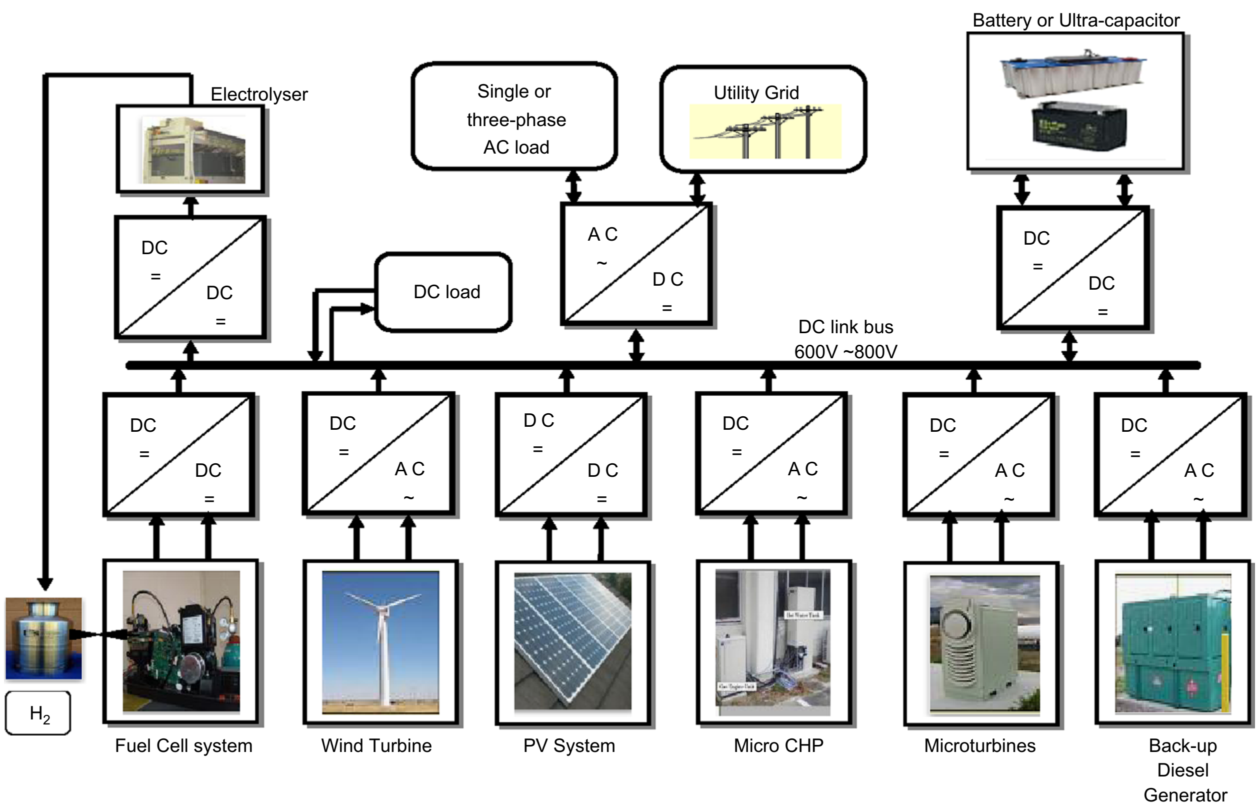


Fig. 1. Basic configuration of the DC microgrid system.

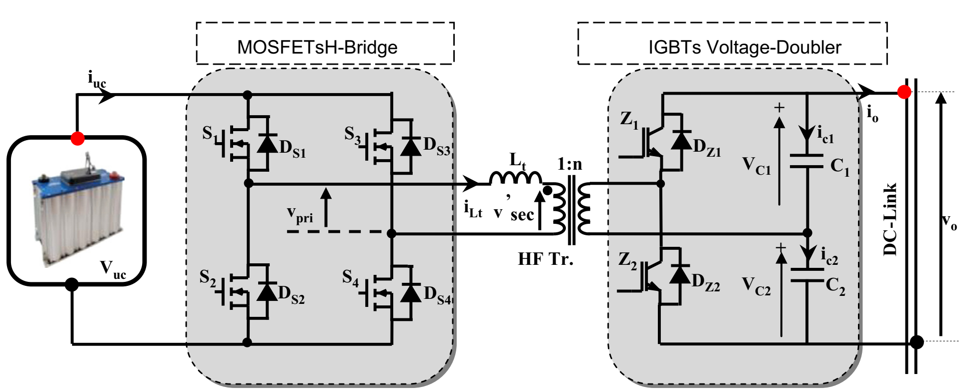


Fig. 2. Schematic of the BDC with voltage-doubler on high-voltage side.

interfacing the UC storage with the renewable sources and the DC link of a DC microgrid. Because the latter has a non-minimum-phase characteristic, the voltage-fed BDC is better suited for dealing with the fast transient power changes due to variable loads. By combining the voltage-fed BDC with a voltage-doubler circuit, as shown in Fig. 2, a converter with a lower number of active devices at the lowest voltage rating and further efficiency improvement can be realised. Therefore, for further investigation of the behaviour of the BDC with the conventional phase-shift control modulation, this topology has been used in this paper.

Typically voltage-fed BDCs use a phase-shift control strategy (presented in Section 2) to control the transfer of power in both directions. However, the BDC operation with a phase-shift control cannot maintain soft-switching (SSW) for a wide UC voltage variation (the output voltage of the UC energy buffer varies widely compared to the batteries, typically between 24 V to 48 V for the Maxwell BoostcapTM ultracapacitor Model BMOD0165 (165 F, 48 V)) and exhibits a higher circulating power flow, a higher RMS current and higher conduction losses as a consequence. Therefore, alternative modulation methods for the BDC are necessary.

In this paper, a comprehensive overview of different modulation methods to control the power flow of the bidirectional voltage-fed DC–DC converter for the UC applications is presented. A detailed analysis of the BDC exploring the impact of the circulating power flow interval is developed in this paper. Analytic methods have been applied to establish alternative modulation methods for the BDC to improve its performance and efficiency.

2. Working principle of BDC

In principle, the isolated BDC can be represented as two DC–AC converters C_A and C_B connected to two DC sources V_A and V_B and interfaced through an inductor L_t as illustrated in Fig. 3a. In order to transfer power, the instantaneous output voltages v_A and v_B must be supplied by the converters C_A and C_B to the inductor L_t (consisting of the transformer leakage inductance plus a possible external inductance). Hence, the BDC can be replaced by two independent AC voltage sources v_A and v_B connected through inductor L_t as shown in Fig. 3b.

To clarify the BDC operation, the voltage and current relationships of the BDC can be analysed using the phasor diagram of the fundamental components, depicted in Fig. 3c.

Based on the fundamental components, the fundamental power flow between the two AC sources in Fig. 3c can be written as

$$P_{AB} = \frac{\hat{V}_{A1}\hat{V}_{B1}}{2X_{Lt}} \sin\varphi \tag{1}$$

where $\hat{V}_{A1}$ and $\hat{V}_{B1}$ are the amplitudes of the fundamental voltages of v_A and v_B, φ is the phase-shift between v_A and v_B, and $X_{Lt}=\omega L_t$.

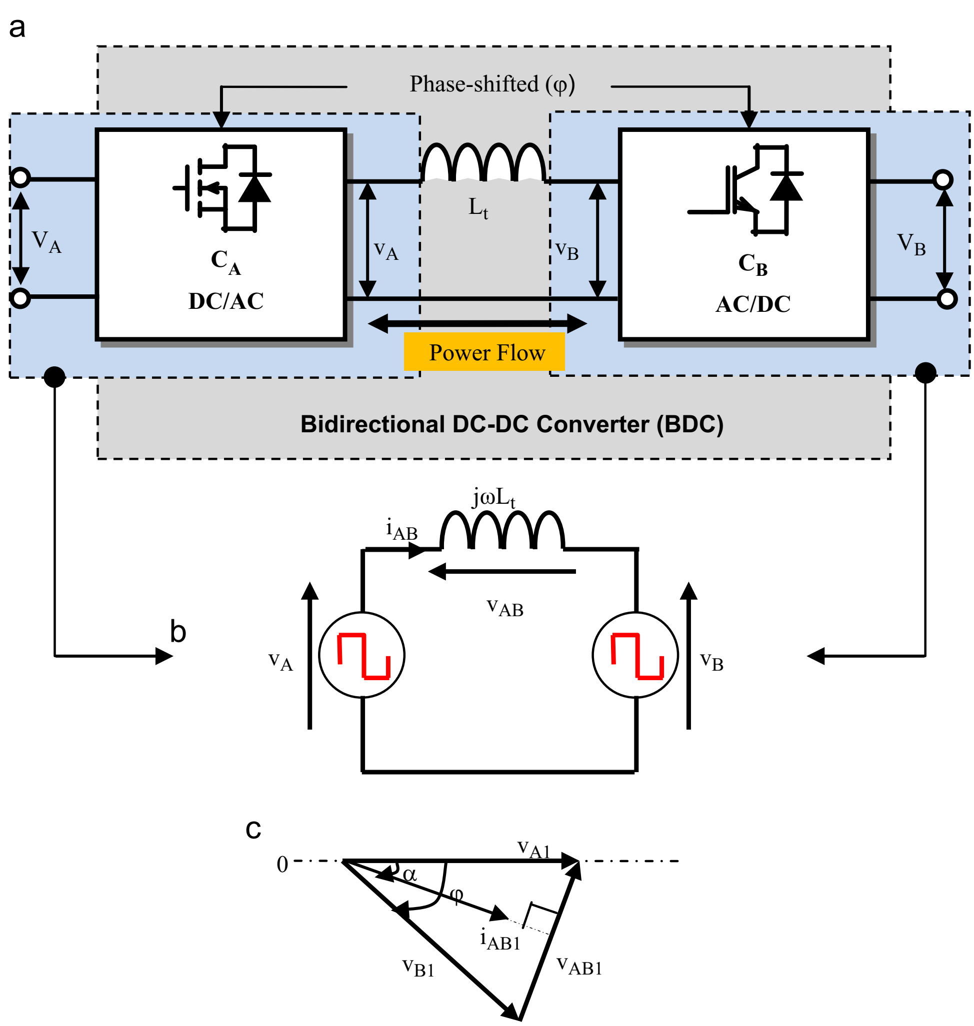


Fig. 3. Operating principle operation of a BDC (a) simplified block diagram, (b) equivalent circuit model and (c) phasor diagram of the fundamental components of the voltage and current.

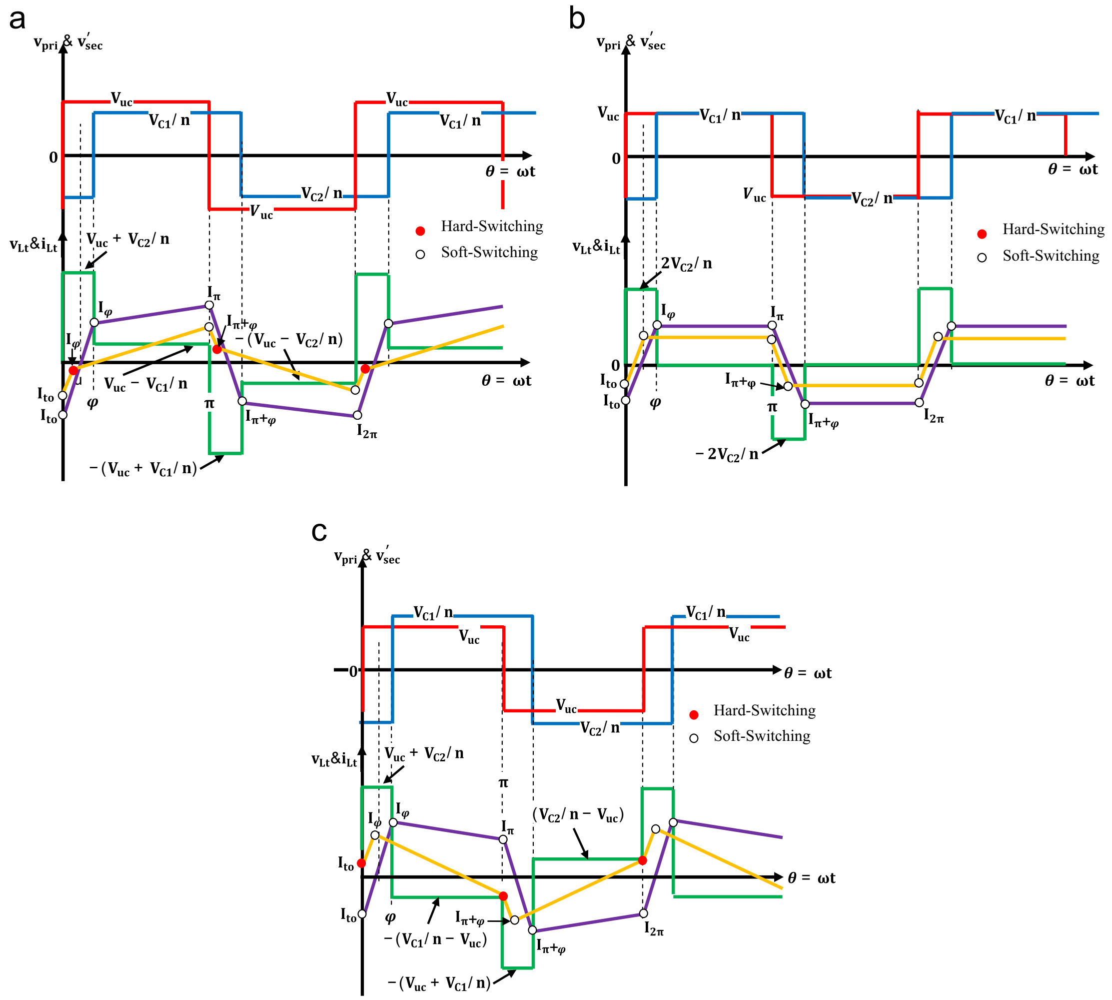


Fig. 4. Voltage and current waveforms of the BDC, operating under UCDM with CPC at different UC voltages: (a) $2nV_{uc}>V_o$, (b) $2nV_{uc}=V_o$, and (c) $2nV_{uc}<V_o$ (Note: yellow and purple waveforms are the primary current plotted for the same V_{uc} and V_o but at different phase-shift angle φ). (For interpretation of the references to colour in this figure legend, the reader is referred to the web version of this article.)

For a square waveform: $\hat{V}_{A1}=\frac{4V_A}{\pi}$ and $\hat{V}_{B1}=\frac{4V_B}{\pi}$.

Referring to (1) the magnitude and direction of the fundamental power in the BDC is determined by the phase-shift φ. Hence, the power transfers from the source v_A to the source v_B in case v_B is lagging v_A (i.e. φ is larger than 0°) and the power transfer reverses in case v_B is leading v_A (i.e. φ is smaller than 0°).

3. Conventional phase-shift modulation scheme

According to Section 2, the BDC uses the phase-shift φ between the voltages across both sides of the isolation transformer to control the transfer of power through the series inductance L_t in both directions. This type of modulation is called here conventional phase-shift control (CPC) modulation [2,3] (also named "Rectangular Modulation" [4–7]). The power flow directions of the BDC are defined as

- *Ultracapacitor charging mode* (*UCCM*): where the average power P_{uc} transfers from DC link side to UC side and $P_{uc}<0$, $\varphi<0$.
- *Ultracapacitor discharging mode* (*UCDM*): where the average power P_{uc} transfers from UC side to DC link side and $P_{uc}>0$, $\varphi>0$.

For a constant output voltage V_0 (this assumption is based on the fact that the output of the BDC is connected to a regulated DC link) the primary voltage $v_{pri}(t)$ across the UC side of the transformer, the secondary voltage v'_{sec} referred to the primary, the voltage $v_{Lt}(t)$ across the series inductance L_t, and the primary current $i_{Lt}(\theta)$ will have the waveforms depicted in Fig. 4 for different UC voltages. In this figure it is assumed that the BDC is operating under CPC and is transferring power from the UC to the DC link (i.e. UCDM).

As can be seen in Fig. 4a–c, when using CPC all BDC switches are driven at 50% duty cycle and the transferred power is controlled by the phase-shift φ only. Hence, the primary voltage $v_{pri}(t)$ is either $+V_{uc}$ or $-V_{uc}$ and the secondary voltage referred to the primary $v'_{sec}(t)$ is either $+V_o/2n$ or $-V_o/2n$ (Note that the principle of operation here is based on the BDC topology shown in Fig. 2). It is obvious that the waveform shape of the primary current $i_{Lt}(\theta)$ is determined by the voltage difference across L_t, i.e. the amplitudes of the UC voltage V_{UC} and DC link voltage $V_0/2n$ referred to the primary.

As can be seen in Fig. 4a–c the waveform of the primary current $i_{Lt}(\theta)$ is symmetrical, hence, only the first half-cycle (time interval T_1: $0<\theta<\varphi$ and time interval T_2: $\varphi<\theta<\pi$) needs to be considered. The equations for the primary current $i_{Lt}(\theta)$ during the first half-cycle for different values of V_{UC} and for both modes (UCCM and UCDM) are given in Table 1. It can be seen that there is only a sign difference between the modes; therefore only the UCDM is considered for the following current and output power calculations. The average power P_{uc} that can be transferred during the

Table 1
Expression for the primary current $i_{Lt(\theta)}$ for different UC voltages in UCCM and UCDM modes.

		$2nV_{uc} > V_o$	$2nV_{uc} = V_o$	$2nV_{uc} < V_o$
UCDM	T_1	$i_{Lt}(\theta) = \left(\frac{(V_{C2}/n)+V_{uc}}{\omega L_t}\theta\right) + i_{Lt}(0)$	$i_{Lt}(\theta) = \left(\frac{2V_{C2}}{n\omega L_t}\theta\right) + i_{Lt}(0)$	$i_{Lt}(\theta) = \left(\frac{(V_{C2}/n)+V_{uc}}{\omega L_t}\theta\right) + i_{Lt}(0)$
	T_2	$i_{Lt}(\theta) = \left(\frac{V_{uc}-(V_{C1}/n)}{\omega L_t}(\theta-\varphi)\right) + i_{Lt}(\varphi)$	$i_{Lt}(\theta) = i_{Lt}(\varphi) = i_{Lt}(\pi)$	$i_{Lt}(\theta) = \left(-\frac{(V_{C1}/n)-V_{uc}}{\omega L_t}(\theta-\varphi)\right) + i_{Lt}(\varphi)$
UCCM	T_1	$i_{Lt}(\theta) = -\left(\frac{(V_{C1}/n)+V_{uc}}{\omega L_t}\theta\right) - i_{Lt}(0)$	$i_{Lt}(\theta) = -\left(\frac{2V_{C2}}{n\omega L_t}\theta\right) - i_{Lt}(0)$	$i_{Lt}(\theta) = -\left(\frac{(V_{C1}/n)+V_{uc}}{\omega L_t}\theta\right) - i_{Lt}(0)$
	T_2	$i_{Lt}(\theta) = -\left(\frac{V_{uc}-(V_{C1}/n)}{\omega L_t}(\theta-\varphi)\right) - i_{Lt}(\varphi)$	$i_{Lt}(\theta) = -i_{Lt}(\varphi) = -i_{Lt}(\pi)$	$i_{Lt}(\theta) = -\left(-\frac{(V_{C1}/n)-V_{uc}}{\omega L_t}(\theta-\varphi)\right) - i_{Lt}(\varphi)$

UCDM can be given as

$$P_{uc} = \frac{2}{2\pi}\int_0^{\pi} v_{pri}(t) i_{Lt}(t)\mathrm{d}t = \frac{V_{uc}}{\pi}\int_0^{\pi} i_{Lt}(t)\mathrm{d}t \tag{2}$$

Thus, to compute the transferred power P_{uc} the current $i_{Lt}(\theta)$ is required. Using the triangular and trapezoidal area calculation methods, the transferred power P_{uc} during the UCDM when $2nV_{uc} > V_o$ can be found as

$$P_{uc} = \frac{V_{uc}}{2\pi}((I_{to} + I_{\varphi})\varphi + (I_{\varphi} + I_{\pi})(\pi - \varphi)) \tag{3}$$

where the current values of I_{to}, I_{φ}, and I_{π} at the commutation instants 0, φ, and π are given as

$$I_{to} = -\frac{(-\pi + \varphi)V_{C1} + \varphi V_{C2} + n\pi V_{uc}}{2n\omega L_t} \tag{4}$$

$$I_{\varphi} = \frac{(\pi - \varphi)V_{C1} + \varphi V_{C2} - n(\pi - 2\varphi)V_{uc}}{2n\omega L_t} \tag{5}$$

and

$$I_{\pi} = -I_{to} = \frac{(-\pi + \varphi)V_{C1} + \varphi V_{C2} + n\pi V_{uc}}{2n\omega L_t} \tag{6}$$

A similar procedure can be applied to find I_{to}, I_{φ}, and I_{π} for $2nV_{UC} < V_o$ or $2nV_{UC} = V_o$.

Using (3)–(6), the transferred average power P_{uc} of the BDC under CPC for the UCDM operation and for $V_{C1} = V_{C2} = V_o/2$ can be given as

$$P_{uc} = \frac{V_o V_{uc}}{2n\pi\omega L_t}(\pi - \varphi)\varphi \tag{7}$$

By equating the derivative of (7) to zero the phase-shift angle φ_{max}^{CPC} for maximum power transfer is found equal to $\pi/2$. Hence, the maximum power $P_{uc_max}^{CPC}$ that can be delivered by the BDC under CPC is

$$P_{uc_CPC}^{max} = \frac{\pi V_o V_{uc}}{8n\omega L_t} \tag{8}$$

Fig. 5 shows the achievable power transfer for the BDC under CPC when the UC voltage changing between 100% and 50% of its rated voltage (see Section 1). It can be seen that BDC under CPC has the ability to deliver power beyond φ_{max}^{CPC} but at the expense of high circulating current through the switches, and higher conduction losses as a consequence. At the phase-shift $\varphi = 180^{\circ}$ the power delivered by the BDC under CPC is 0 W. It should be noted that in practice the converter is not able to deliver 0 W due to the effect of the fall and rise time of the gate signals [8]. Eq. (8)shows that the maximum achievable power P_{uc}^{max} is not only limited by the maximum phase-shift angle but also by the series inductance L_t and the transformer turns ratio n. Hence, L_t and n must be selected based on the required rated power for the BDC with respect to the lowest RMS current.

3.1. SSW analysis

From (7), it is evident that the power of the BDC under CPC can be controlled by varying φ only and for that reason the CPC

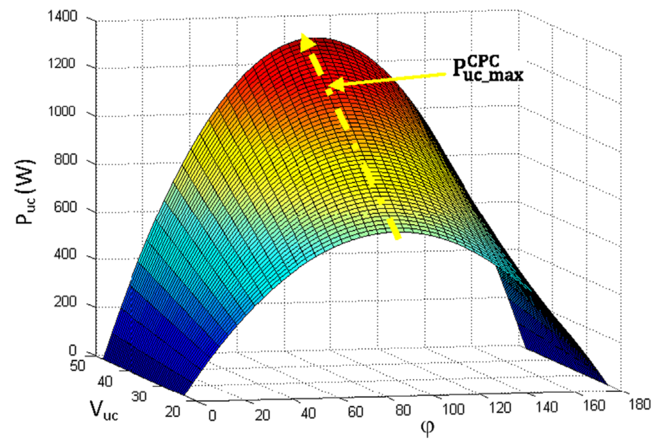


Fig. 5. 3D contour surfaces of the BDC power flow under CPC modulation ($L_t = 10$ μH, $n = 7.4$, $V_o = 650$V, and $f_s = 20$ kHz).

modulation method has been used widely [3,4,9], because of its simplicity of implementation. In addition, the BDC under CPC has the highest power transfer capability of any modulation scheme [10,11]. Also, one of the CPC advantages is that the switching devices at both BDC sides are capable of operating with zero-voltage switching (ZVS) for the entire phase-shift angle range (see Fig. 4b). However, this is only possible when the following conditions are valid:

$$I_{to} < 0,\ \ I_{\varphi} > 0,\ \ I_{\pi} > 0,\ \text{ and }\ I_{\pi+\varphi} < 0 \tag{9}$$

The above SSW conditions mean that the values of the currents (I_{to}, I_{φ}, I_{π}, and $I_{\pi+\varphi}$) at the switching instants 0, φ, π, and $\pi+\varphi$ must be sufficient to discharge and charge the parasitic capacitances of the switches (S_1–S_2, Z_1, S_3–S_4, and Z_2) during the dead periods in order to ensure zero-volts before the switches are conducting (see purple and yellow waveforms in Fig. 4a–c). Fig. 6 details what the required amount of these currents I_{to}, I_{ϕ}, I_{π} and $I_{\pi+\varphi}$ is to ensure ZVS for the BDC switches S_1–S_2, Z_1, S_3–S_4, and Z_2 respectively. Note that Fig. 6a–d is plotted for the wide variation in the UC voltage over the entire power range.[1]

From Fig. 6a it can be seen that when the UC voltage is low (i.e. $2nV_{uc} < V_o$ the value of the current I_{to}) is not sufficient to discharge the parasitic capacitances of the diagonal switches S_1–S_2 at medium and light loads. Thus, S_1–S_2 is operating under hard switching (HSW) for this load and UC voltage range. In contrast, when the UC voltage increases (i.e. $2nV_{uc} > V_o$) the value of the current I_{φ} is not sufficient to discharge the parasitic capacitances of the switch Z_1, resulting in a failure to realise ZVS for Z_1 under light load, as indicated in Fig. 6b. Similar to Fig. 6a, Fig. 6c shows that ZVS is not realised for the other diagonal switches S_3–S_4 at the switching instant π when $2nV_{uc} < V_o$ due to the small value of the current I_{π}.

[1] The available power range is dependent to the entire allowable phase-shift φ in the CPC, as shown in Fig. 5.

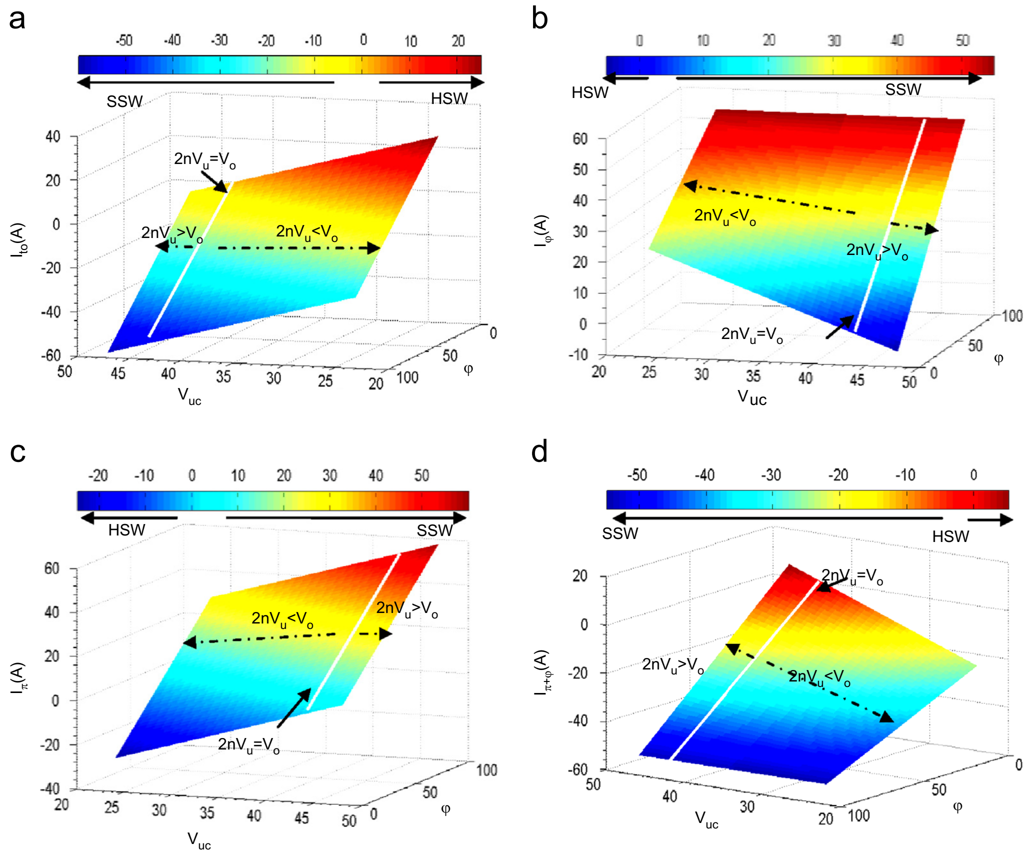


Fig. 6. 3D contour surface shows the available current via the series inductance L_t at the commutation instants 0, φ, π, and $\pi+\varphi$: (a) I_{to}, (b) I_{φ}, (c) I_{π} and (d) $I_{\pi+\varphi}$.

ZVS for the voltage-doubler switch Z_2 fails at the turn-on instant $\pi+\varphi$ when $2nV_{uc}<V_o$, as shown in Fig. 6d. This is due to insufficient energy available from the series inductance L_t (i.e. $I_{\pi+\varphi}>0$) to discharge the parasitic capacitance of Z_2.

However, it can be noted that SSW operation is only possible when the amplitude of the secondary voltage reflected at the primary $v'_{sec}(t)$ is equal to the amplitude of the UC voltage V_{uc} (i.e. $2nV_{uc}=V_o$, see the white lines in Fig. 6a–d) and both voltages remain essentially constant (e.g. fixed-voltage DC–DC converters or battery chargers/dischargers). Thus, the BDC operating under CPC has a limited soft-switching range when operated with sources that have a wide input voltage variation, such as UCs.

Another disadvantage of the CPC method is that it increases the RMS current and the conduction loss in the BDC parts. This can be clarified as described next.

3.2. RMS analysis

The RMS primary current I_{rms} through the BDC when it is operating under CPC in UCDM is given as

$$I_{rms}=\sqrt{\frac{1}{2\pi}\left[\int_0^{2\pi} i_{Lt}^2(\theta)\,d\theta\right]} \tag{10}$$

Using Eqs. (4)–(6) and Table 1, the RMS current when $2nV_{uc}=V_o$ and $2nV_{uc}>V_o$ respectively are given as

$$I_{rms}=\frac{\sqrt{3\pi-2\varphi}}{\sqrt{3\pi}}\frac{V_o}{2n\omega L_t}\varphi \tag{11}$$

and

$$I_{rms}=V_o\frac{\sqrt{(7\pi^3-24\pi^2\varphi+30\pi\varphi^2-12\varphi^3)}}{4n\sqrt{3\pi}\omega L_t}$$
$$+\frac{\sqrt{n(-7\pi^3+18\pi^2\varphi-12\pi\varphi^2+2\varphi^3)V_oV_{uc}}}{2n\sqrt{3\pi}\omega L_t}$$
$$+V_{uc}\frac{\sqrt{\pi(7\pi^2-12\pi\varphi+6\varphi^2)}}{2\sqrt{3\pi}\omega L_t} \tag{12}$$

From (7), the required series inductance L_t can be obtained as

$$L_t=\frac{V_oV_{uc}}{2n\pi P_{uc}\omega}(\pi-\varphi)\varphi \tag{13}$$

Substitute (13) in (11) and (12), the relation between the RMS current I_{rms}, the transferred power P_{uc}, and the phase-shift φ is given as

$$I_{rms}=\frac{\pi\sqrt{1-(2\varphi/3\pi)}}{(\pi-\varphi)V_{uc}}P_{uc} \tag{14}$$

and

$$I_{rms}=\sqrt{\frac{\pi}{3}}\frac{P_{uc}}{2(\pi-\varphi)\varphi V_oV_{uc}}\Big(V_o\sqrt{(7\pi^3-24\pi^2\varphi+30\pi\varphi^2-12\varphi^3)}$$
$$+2\sqrt{nV_oV_{uc}(-7\pi^3+18\pi^2\varphi-12\pi\varphi^2+2\varphi^3)}$$
$$+2nV_{uc}\sqrt{\pi(7\pi^2-12\pi\varphi+6\varphi^2)}\Big) \tag{15}$$

for $2nV_{uc}=V_o$ and $2nV_{uc}>V_o$ respectively.

The relationships (14) and (15) between the primary RMS current and the phase-shift φ for the two cases at the same power are shown in Fig. 7.

It is clear that the RMS current of the BDC under CPC increases at higher φ values and that the BDC has a higher RMS current when the UC voltage increases (i.e. $2nV_{uc}>V_o$). Thus, from the view of higher efficiency it is desirable for the BDC under CPC to operate: (i) with the smallest phase-shift φ and (ii) when

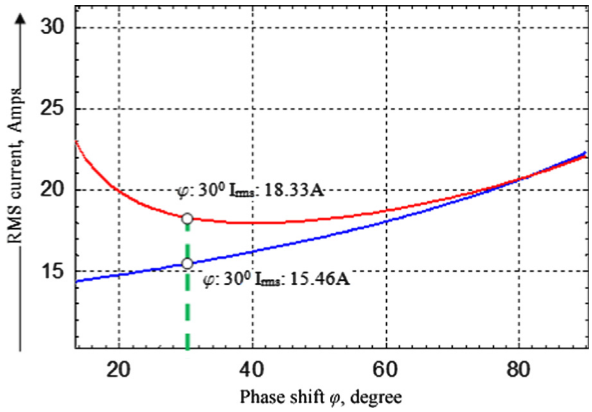


Fig. 7. Primary RMS current when $2nV_{uc} > V_o$ (red) and $2nV_{uc} = V_o$ (blue) ($P_{uc} = 600$ W, $V_o = 650$ V, $n = 7.4$, and $f_s = 20$ kHz).

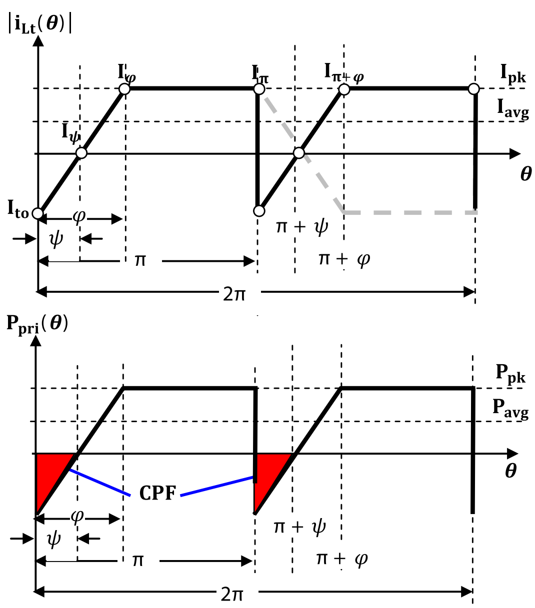


Fig. 8. Primary current (top) and instantaneous power flow (bottom) of the BDC for $P_{uc} > 0$ for arbitrary φ.

$2nV_{uc} = V_o$. However, this is at the detriment of the power transfer capability of the BDC and its use in UC applications.

3.3. Circulating power flow (CPF) analysis

Due to the series inductance L_t the primary and secondary currents lag their voltage by an angle that varies with the required power. Consequently, part of the absorbed power is circulating through the converter and flows back to the input source. This is shown in Fig. 8 (bottom waveform) for the BDC operating with CPC, where the instantaneous power at the primary $P_{pri}(\theta)$ is plotted for one full cycle of the converter operation for an arbitrary phase-shift angle φ. The interval denoted by ψ is defined here as the CPF interval and is related to the power required by the load. To find a mathematical expression representing the CPF interval, the absolute value of the primary current $|i_{Lt}(\theta)|$ waveform is also plotted in Fig. 8 (top waveform). For simplification, the waveforms are plotted for $2nV_{uc} = V_o$. Notice that the average value of the primary current $i_{Lt}(\theta)$ is equal to zero over the full-cycle. Thus, for

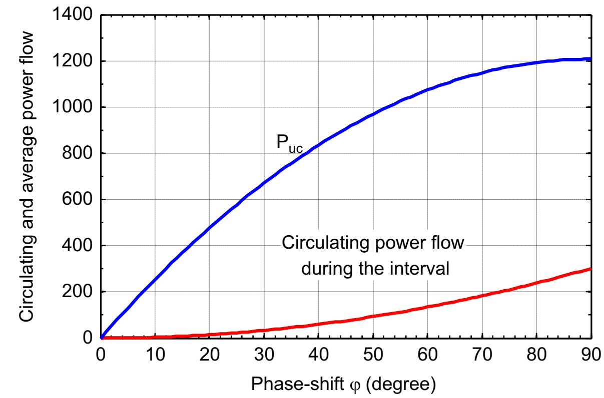


Fig. 9. Average power flow (blue line) and circulating power flow of the BDC operating under CPC at $2nV_{uc} = V_o$ and UCDM. (For interpretation of the references to colour in this figure legend, the reader is referred to the web version of this article.)

the first half-cycle the current for each interval can be obtained as

$$i_{Lt}(\theta) = \begin{cases} \frac{V_o}{\omega L_t}\theta + I_{to} & 0 \le \theta \le \varphi \\ I_\varphi = I_\pi & \varphi \le \theta \le \pi \end{cases} \tag{16}$$

The values of the currents I_{to} and I_φ at the commutation instants 0 and φ are given as

$$I_{to} = -\frac{V_o}{2n\omega L_t}\varphi \tag{17}$$

and

$$I_\varphi = \frac{V_o}{2n\omega L_t}\varphi \tag{18}$$

Using (17), the CPF (the red area in Fig. 8) is obtained as

$$\text{CPF} = -\frac{V_o V_{uc}}{8\pi n \omega L_t}\varphi^2 \tag{19}$$

Obviously, the CPF is zero when $\varphi = 0$. This fact is shown in Fig. 9 where the circulating power CPF (red line) with the average power P_{uc} (blue line) is plotted against φ for different angles.

It can be seen that the CPF increases as the phase-shift increases. This means that as the phase-shift is increased in respect to the required output power more circulating energy is freewheeling through the anti-parallel diodes of the MOSFETs and flows back to the input source. Due to the high reverse-recovery charge Q_{rev} of the anti-parallel diodes[2] this energy leads to an increase in reverse-recovery losses[3] as well as conduction losses of the MOSFETs.

The disadvantage of CPC modulation have led many authors to find alternative modulation approaches, seeking to extend the SSW range and improve the performance and the efficiency of the BDC. Some of those approaches are described in the next section.

4. Alternative phase-shift modulation schemes

In the present application, the BDC is needed to connect the UC with the DC link of the DC microgrid. Based on the specifications of the Maxwell Boostcap™ ultracapacitor Model BMOD0165 described in [12], the operating voltage range of this model is between 48 V and 24 V. Thus, the input voltage of the BDC varies significantly. Hence, as clarified in the previous section, due to the

[2] Typically, reverse-recovery charge Q_{rev} for the anti-parallel diode of the bridge MOSFET is 5 μC compared to the 28 nC for the Schottkey diodes used in the voltage-doubler.

[3] The reverse-recovery losses change in relation to the Q_{rev}.

high switching and conduction losses the CPC is not the preferable modulation for the BDC circuit when it is operating with a source with a wide input/output voltage. Therefore, to minimise the losses and improve the BDC performance an alternative modulation is required.

Many topologies have been proposed to minimise the conduction loss and extend the SSW range for the BDC. These topologies can be divided into two main approaches: the first approach is based on using additional components with the BDC such as a resonant circuit, a variable AC link reactance, or a snubber circuit [13,14–20]. While these approaches extend the soft-switching for converter's switches, the result is an increase of the circulating currents, with a higher conduction loss as a consequence, as well as higher converter costs. The second approach is to modify the switching control strategy of the CPC modulation without adding any additional components. This approach is called here the alternative phase-shift modulation (APM). The APM uses the phase-shift between the primary and secondary voltages to deliver the required power while changing the duty cycle of the converter bridges to maximise operating efficiency of the BDC. However, improving the efficiency using this approach is on account of increasing the complexity of implementing the switching controller. Nevertheless, this approach is very smart and therefore has attracted many authors [5,11,21–29] since it minimises the losses without adding more passive or active components.

However, it should be mentioned here that although the BDC with voltage-doubler configuration, shown in Fig. 2, has a number of advantages, but certain APM schemes cannot be applied to the voltage-doubler configuration. For that reason, the two BDC bridges shown in Fig. 10 are considered for further investigation in this section.

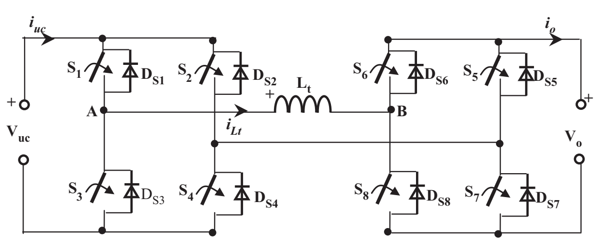


Fig. 10. Schematic diagram of the BDC with two H-bridges.

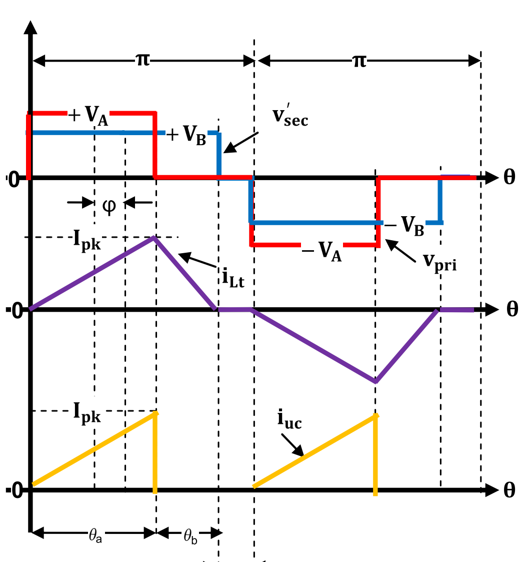


Fig. 11. Key waveforms of the TRM scheme, when $V_A > V_B$ and the BDC under UDCM.

Different APM schemes are described in the following sections.

4.1. Triangular current modulation

In [15,25,28], an APM scheme called triangular current modulation (TRM) is proposed to reduce the circulating current through the converter by shaping the current in the primary winding to a triangular waveform, where the two BDC bridges shown in Fig. 10 are driven with a variable duty cycle. The key waveforms of this modulation scheme are shown in Fig. 11 where the operational modes of the BDC under TRM and $V_A > V_B$ can be divided into six modes over one cycle.

The two half cycles are complementary. Unlike CPC, the states of the primary voltage $v_{pri}(t)$ over one cycle fluctuates as ($+V_A$, 0, 0, $-V_A$, 0, 0) and the state of the secondary voltage $v'_{sec}(t)$ fluctuates as ($+V_B$, $+V_B$, 0, $-V_B$, $-V_B$, 0), where the voltages V_A ($V_A = V_{uc}$) and V_B ($V_B = V_o/n$) are the amplitude of the $v_{pri}(t)$ and $v'_{sec}(t)$ respectively. Hence, the primary current i_{Lt} during the periods θ_a, θ_b, and θ_c can be given as

$$i_{Lt}(\theta) = \begin{cases} \frac{V_A - V_B}{\omega L_t}\theta & 0 < \theta < \theta_a \\ \frac{-V_B}{\omega L_t}(\theta - \theta_a) + i_{Lt}(\theta_a) & \theta_a < \theta < \theta_b \\ 0 & \theta_b < \theta < \theta_c \end{cases} \tag{20}$$

Using Fig. 11 and (20), the transferred power P_{uc} when $V_A > V_B$ and the BDC operates in UCDM is given by

$$P_{uc} = \frac{V_A(V_A - V_B)\theta_a^2}{2\pi\omega L_t} \tag{21}$$

By applying the volt-second balance principle across the L_t during the first half-cycle the relation between the angles θ_a and θ_b can be obtained as

$$\theta_a = \frac{V_B}{(V_A - V_B)}\theta_b \tag{22}$$

where θ_b is given by

$$\theta_b = 2\varphi \tag{23}$$

where φ represents the angle difference between the centres of the voltage pulses across the primary and secondary.

Then, the transferred power P_{uc}^{TRM} in relation to φ when $V_A > V_B$ is given as

$$P_{uc}^{TRM} = \frac{2\varphi^2 V_A V_B^2}{\pi\omega L_t(V_A - V_B)} \tag{24}$$

At the maximum power possible with the TRM the sum of θ_a and θ_b is equal to the duration of one half-cycle π and the period $\theta_c = 0$.[4] Hence, the period θ_b is equal to ($\pi - \theta_a$). Based on that, the maximum phase-shift φ_{max}^{TRM} that maintains a triangular shape for the primary current and makes $I(\theta_b)$ equal to zero (see purple waveform in Fig. 11) is given as

$$\varphi_{max}^{TRM} = \frac{1}{2}\frac{\pi(V_A - V_B)}{V_A} \tag{25}$$

Substituting (25) in (24) the maximum power $P_{uc_max}^{TRM}$ that can be transferred under TRM when $V_A > V_B$ and the BDC in UCDM found as

$$P_{uc_max}^{TRM} = \frac{\pi V_B^2}{2\omega L_t V_A}(V_A - V_B) \tag{26}$$

[4] Note that the duration of the periods θ_b and θ_c are controlled by changing the duty cycle of the DC link bridges.

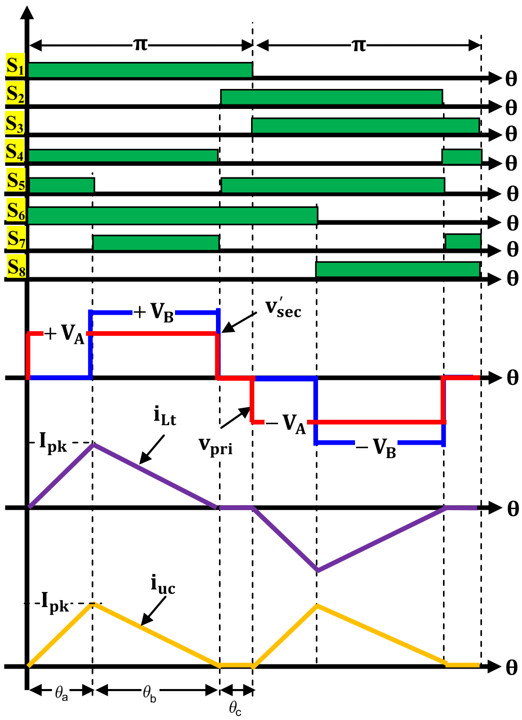


Fig. 12. Gate signals, transformer voltages, primary current, and input current waveforms for TRM, when $V_A < V_B$ and the BDC in UDCM.

From (26), it is obvious that

$$P_{uc_{max}}^{TRM} = \begin{cases} + & for \quad V_A > V_B \\ 0 & for \quad V_A = V_B \\ - & for \quad V_A < V_B \end{cases} \tag{27}$$

thus, when $V_A < V_B$ and $V_A = V_B$ the TRM cannot be used. TRM only permits a positive power transfer when $V_A > V_B$ and the BDC is in UCDM. Thus, the BDC operating under TRM requires a higher transformer turns ratio n. Hence, n should be designed as

$$n > \frac{V_o}{V_{uc_min}} \tag{28}$$

A high turns ratio means that less power will be transferred by the BDC for the same φ.

TRM operation with $V_A < V_B$ can be achieved if the $v_{pri}(t)$ and $v'_{sec}(t)$ waveforms are modified to be aligned at the falling-edge, as shown in Fig. 12 [23,28]. In this case θ_a, θ_b and θ_c must be recalculated by driving the bridge switches with a duty cycle different from that used for $V_A > V_B$. This means further complexity added to the implementation of the switching control.

4.2. Modified triangular current modulation

To extend the range of the TRM operation so that it can be used even when $V_A = V_B$, a modified TRM scheme called a "proposed TRM" (PTRM) was presented in [22]. As shown in Fig. 13, in this scheme the voltages V_A and V_B are arranged so there is no overlap. With the PTRM the primary current still keeps its triangular shape by selecting θ_a to be ≤(θ_b+θ_c) over the entire load range. Hence, the primary current i_{Lt} during the periods θ_a, θ_b, and θ_c can be given as

$$i_{Lt}(\theta) = \begin{cases} \frac{V_A}{\omega L_t}\theta & 0 < \theta < \theta_a \\ \frac{-V_B}{\omega L_t}(\theta - \theta_a) + i_{Lt}(\theta_a) & \theta_a < \theta < \theta_b \\ 0 & \theta_b < \theta < \theta_c \end{cases} \tag{29}$$

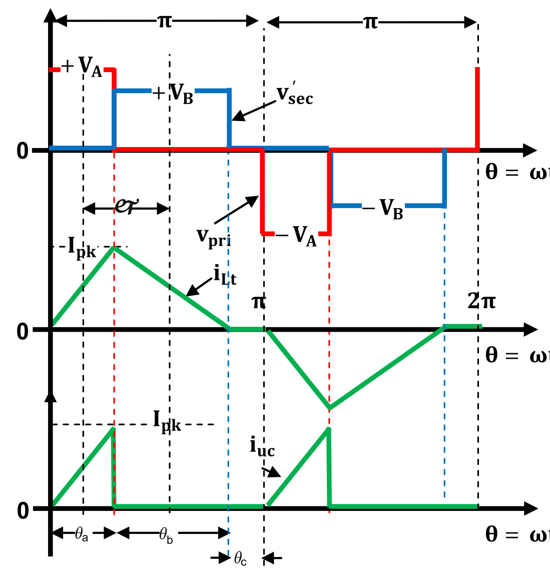


Fig. 13. Key waveforms of PTRM approach for $V_A > V_B$ with the BDC operating in UCDM.

Using (29) and Fig. 13, the achievable transferred power by the PTRM can be obtained as

$$P_{uc}^{PTRM} = \frac{V_A^2 \theta_a^2}{2\pi\omega L_t} \tag{30}$$

From Fig. 13, the relation between θ_a, θ_b and φ (which is defined in Section 4.1) is given as

$$\theta_b = 2\varphi - \theta_a \tag{31}$$

where

$$\theta_a = \frac{2\varphi V_B}{V_A + V_B} \tag{32}$$

Substituting (32) in (30), the transferred power P_{uc}^{PTRM} in relation to φ is

$$P_{uc}^{PTRM} = \frac{2\varphi^2 V_A^2 V_B^2}{\pi\omega L_t (V_A + V_B)^2} \tag{33}$$

Using the same procedure shown for TRM, the maximum phase-shift φ_{max}^{PTRM} and the maximum transferrable power $P_{uc_max}^{PTRM}$ under PTRM are obtained as

$$\varphi_{max}^{PTRM} = \pi/2 = \theta_a = \theta_b \tag{34}$$

and

$$P_{uc_max}^{PTRM} = \frac{\pi V_A^2 V_B^2}{2\omega L_t (V_A + V_B)^2} \tag{35}$$

Unlike conventional TRM, it is clear from (35) that the PTRM scheme permits a positive power transfer for the UCDM for any V_A and V_B values. However, this scheme has the drawback of high RMS and peak currents and can therefore be used only at light load.

A modified triangular current modulation (MTRM) is proposed in [21,30]. In this method the duty cycles of both bridges are varied between 0% and 50% in relation to the amount of the phase-shift φ. The key waveforms of MTRM are shown in Fig. 14.

With MTRM, ZCS is realised for the UC bridge switches which reduces the circulating current. However, this is possible only at light load, as shown in Fig. 14b [21,30], and does not reduce the circulating current at the medium and high load. In addition it reduces the BDC power capability since it does not use a phase shift between the bridges but only changes the RMS voltage across

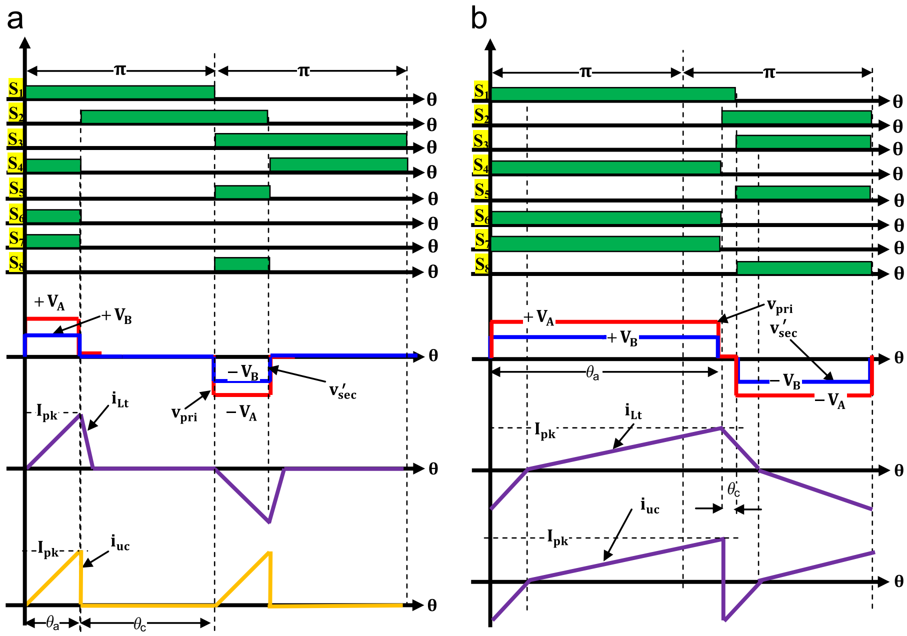


Fig. 14. Key waveforms of MTRM approach for $V_A > V_B$ with the BDC operating in UCDM.

the bridges to control the power flow. Furthermore, asymmetrical voltage waveforms across the transformer can result in magnetic saturation of the transformer due to voltage–time imbalance.

4.3. Hybrid modulation schemes

With the TRM, PTRM, and MTRM the soft-switching operation range for the BDC can be significantly improved and the conduction losses reduced, but the penalty is that the maximum transferrable power is far below the maximum possible power of the BDC, making them undesirable for use in high power applications.[5] Therefore, several methods have been proposed in the literature to combine the above schemes with other modulations so that the full power capability of the BDC can be exploited. These methods are described below.

4.3.1. PTRM–CPC hybrid modulation

A hybrid modulation for the BDC, based on a combination of a PTRM scheme (see Fig. 13) and CPC modulation (see Fig. 4), was presented in [22]. In PTRM–CPC the BDC operates with PTRM only for low power transfer while the CPC used for high power transfer, since the PTRM is not suitable for high power operation as mentioned before. Thus, with PTRM–CPC the BDC is operating under CPC for most of the power range, which is not preferable when the input voltage varies significantly, as indicated in Section 3. Furthermore, because the primary current is not zero at the transition from PTRM to CPC mode high peak currents could be incurred. Thus, to protect the BDC from high peak current at the mode transition a hysteresis comparator is required.

4.3.2. TRM–TZM hybrid modulation

In [15,23,28] a combination of TRM with the trapezoidal current modulation (TZM) is proposed. In this method the BDC is

[5] Using these schemes for the high power range increases the peak current stress and the conduction loss in the BDC switches, thus, reducing the efficiency.

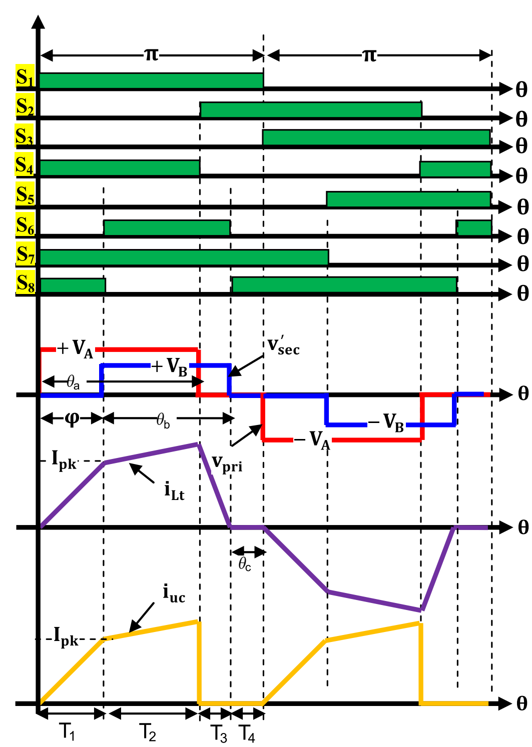


Fig. 15. Key waveforms of TZM approach for $V_A > V_B$ with the BDC operating in UCDM.

operating under TRM up to half-load after which TZM is employed. The key waveforms of the TZM scheme are depicted in Fig. 15.

The operational modes of the BDC under the TZM scheme can be divided into eight intervals over one switching cycle, as shown in Fig. 15. Compared to the CPC (see Fig. 4c), TZM imposed zero current through the transformer by applying a zero voltage across both bridge sides during the interval T_4. The primary current $i_{Lt}(\theta)$ during the first half-cycle (i.e. T_1, T_2, T_3 and T_4), when $V_A > V_B$ and

Table 2
Comparison between different modulation schemes for BDC.

APM scheme	RMS current in the BDC	SSW status	Power transfer capability P_{uc_max}	Switching controller complexity	Limits
CPC	High	ZVS for all switches (only if $V_A = V_B$)	High (under the BDC power rating)	Very low (fixed duty cycle with variable phase-shift)	
TRM	Low (if operating with power rating less than TZM range)	ZVS and ZCS for all switches	Low (less than the achievable power of TZM), where the maximum power $P^{TRM}_{uc_max}$ that can be transferred is $P^{TRM}_{uc_max} = \frac{\pi V_B^2}{2\omega L_t V_A}(V_A - V_B)$	Very high (variable duty cycle with phase-shift, rising-edge and falling edge alignment required)	Does not work if $V_A = V_B$ and $V_A < V_B$. High n required
PTRM	Low (if operating under light load)	ZCS for all switches	Medium (higher than TRM and less than TZM) when $P^{PTRM}_{uc_max} = \frac{\pi V_A^2 V_B^2}{2\omega L_t (V_A + V_B)^2}$	High (fixed duty cycle with variable phase-shift)	Limits the duty cycle for both bridges to less than 25%
MTRM	Medium (at the light load), high (for the high power transfer)	ZCS for all switches when BDC operating under light load only	Medium	Medium (variable duty cycle with fixed phase-shift)	
TZM	Lower than CPC within same operating range, higher than TRM	ZVS and ZCS for all switches	High but $< P^{CPC}_{uc_max}$	High (variable duty cycle with phase-shift)	
VSB	Medium if $V_{uc} > V_{uc_min}$, high if $V_{uc} = V_{uc_min}$	ZVS if $V_{uc} > V_{uc_min}$	High only if $V_{uc} = V_{uc_min}$	Medium (variable duty cycle with phase-shift only if $V_{uc} > V_{uc_min}$)	High n required

the BDC operates under UCDM, is described by

$$i_{Lt}(\theta) = \begin{cases} \frac{V_A}{\omega L_t}\theta & \text{for all } \theta \in T_1 \\ \frac{V_A - V_B}{\omega L_t}(\theta - \varphi) + i_{Lt}(\varphi) & \text{for all } \theta \in T_2 \\ \frac{-V_B}{\omega L_t}(\theta - \theta_a) + i_{Lt}(\theta_a) & \text{for all } \theta \in T_3 \\ 0 & \text{for all } \theta \in T_4 \end{cases} \quad (36)$$

Using (36) the transferred power that can be delivered by the BDC under TZM is given as

$$P^{TZM}_{uc} = \frac{V_A}{2\pi\omega L_t}(V_A\theta_a^2 - V_B(\varphi - \theta_a)^2) \quad (37)$$

With the TRM–TZM hybrid modulation the efficiency of the BDC is considerably improved compared to the PTRM–CPC hybrid modulation but the current through the primary winding becomes discontinuous over the entire power range which is not appropriate in most applications due to the higher device current stresses. In addition, the maximum power achieved by the BDC under the TRM–TZM is less than the maximum power capabilities of the CPC and the PTRM–CPC modulations.

4.3.3. TRM–TZM–CPC combination

Further efficiency enhancements were developed by a combination of TRM, TZM, and CPC modulation schemes so that the appropriate scheme is selected based on the required output power [5]. Compared to the TRM–TZM hybrid modulation, combining TRM and TZM with the CPC modulation increases the power capability of the BDC and improves the efficiency over the entire range. However, the transition between TRM (for a medium power operation) and CPC (for a high power operation) causes a high crest factor current which increases the complexity of the controller significantly.

4.3.4. Composite dual PWM scheme

To realise ZVS down to light-load and to reduce circulating energy, a composite scheme based on selecting either dual PWM for the low power transfer operation or a single PWM for high power transfer operation is presented in [31]. For the high power transfer the BDC operates with the modulation proposed in [27], where PWM used in addition to the CPC modulation. Using this scheme, maximum efficiency occurs only in the light load range.

In addition to the above modulations and combination methods, other modulations have been proposed that achieve lower switching losses based on optimum selection of the duty cycles in respect to the phase-shift angle, such as described in [25,32,33,34,]. Based on the BDC loss model, an accurate mathematical analysis has been achieved in [25] to calculate the required phase-shift angle and the duty cycle that result in minimisation of the peak currents and switching losses in the converter. However, this modulation requires a very complex algorithm controller to generate the required phase-shift and duty cycle especially when the input and the output sources have wide voltage variation. In addition, it does not reduce the circulating energy and it restricts the converter power capability.

4.4. Voltage-balance modulation scheme

Ref. [32] proposes a duty ratio modulation scheme called 'volt-second balance control' (VBC) to improve the soft-switching operation of the BDC. The main idea of VBC modulation is to keep the volt-second product across the transformer winding the same, thus extending the ZVS range of the BDC switches. In this method the duty cycle D has been calculated in respect to the UC voltage as

$$D = \frac{V_{uc_min}}{2V_{uc}} \quad (38)$$

where $V_{uc_min} = 50\%$ of V_{uc}.

Note that at V_{uc_min} the duty cycle $D = 50\%$ but $D = 25\%$ for $V_{uc} = V_{uc_max}$. This choice for duty cycle can provide ZVS for the ultracapacitor bridge side but only for a limited load range. Furthermore, if $V_{uc} = V_{uc_min}$ the BDC has to be operated under CPC for the full power range. Also, the effect of the conduction losses and circulating energy has not been addressed.

5. Conclusions

To control the power flow of the ultracapacitor bidirectional converter a phase-shift between the voltages across both sides of the converter is required. Despite its simplicity of implementation the standard CPC method causes degradation in the performance and operating efficiency of the converter. Therefore, an alternative modulation method to improve the converter performance is necessary. To help designers to choose the optimal modulation scheme for the voltage-fed BDC, a comprehensive overview and detailed analysis for a number of modulation methods to control

the power flow of the BDC with extended soft-switching operation and lower conduction losses has been presented in this paper. The main features of these different modulation schemes for the BDC are summarised in Table 2.

References

[1] Chowdhury S, Chowdhury SP, Crossley P. The Institute of Engineering & Technology. London, United Kingdom: Microgrids and Active Distribution Networks; 2009.
[2] Hatziargyriou ND, Meliopoulos APS. Distributed energy sources: technical challenges. In: Proceedings of IEEE PES winter meeting; 2002. p. 1017–1022.
[3] Kheraluwala MH, Gasgoigne RW, Divan DM, Bauman E. Performance characterization of a high power dual active bridge DC/DC converter. In: Proceedings of IEEE industry applications society annual meeting; 7–12 October, 1990. p. 1267–1273.
[4] Chan HL, Cheng KWE, Sutanto D. A novel square-wave converter with bidirectional power flow. In: Proceedings of IEEE international conference on power electronics and drive systems, PEDS '99; July 1999, p. 966–971.
[5] Wang Y, de Haan SWH, Ferreira JA.. Optimal operating ranges of three modulation methods in dual active bridge converters. In: Proceedings of the 6th IEEE international power electronics and motion control conference (IPEMC '09). China; 17–20 May, 2009. p. 1397–1401.
[6] Kheraluwala MH. High power high frequency DC-to-DC converters. PhD thesis. WI: University of Wisconsin-Madison, USA; 1991.
[7] Haimin T, Kotsopoulos A, Duarte JL, Hendrix MAM. Transformer-coupled multiport ZVS bidirectional DC–DC converter with wide input range. IEEE Transactions on Power Electronics 2008;23:771–81.
[8] Bai H, Mi CC, Gargies S. The short-time-scale transient processes in high-voltage and high-power isolated bidirectional DC–DC converters. IEEE Transactions on Power Electronics 2008;23:2648–56.
[9] Gitaua MN, Ebersohna G, Kettleboroughb JG. Power processor for interfacing battery storage system to 725 V DC bus. Energy Conversion and Management 2007871–81.
[10] Schibli N. Symmetrical multilevel converters with two quadrant DC–DC feeding. PhD thesis. Swiss Federal Institute of Technology, Lausanne; 2000.
[11] Shen Z, Burgos R, Boroyevich D, Wang F, Soft-switching capability analysis of a dual active bridge DC–DC converter. In: Proceedings of IEEE electric ship technologies symposium (ESTS 2009); 20–22 April, 2009. p. 334–339.
[12] Maxwell. DataSheet MC Power Series 48V Modules. Available from: 〈http://www.cdiweb.com/datasheets/maxwell/DATASHEET_48V_series_1009365.pdf〉, [accessed 01.07.10].
[13] Chen W, Wang S, Hong X, Ye ZLS.. Fully soft-switched bidirectional resonant DC–DC converter with a new CLLC tank. In: Proceedings of the 25th annual IEEE applied power electronics conference and exposition (APEC 2010); 21–25 February, 2010. p. 1238–1242.
[14] Isurin A, Cook A.. Achieving a wide input voltage and output power load range step-down DC-DC conversion with good full range efficiency at 4 kW. In: Proceedings of the 21st IEEE annual applied power electronics conference and exposition (APEC 2006); 23 March, 2006. p. 67–71.
[15] Vangen K, Melaa T, Bergsmark S, Nilsen R. Efficient high-frequency soft-switched power converter with signal processor control. In: Proceedings of IEEE telecommunications energy conference (INTELEC '91); 5–8 November, 1991. p. 631–639.
[16] Hua G, Lee FC, Jovanovic MM. An improved full-bridge zero-voltage-switched PWM converter using a saturable inductor. IEEE Transaction on Power Electronics 1993;8:530–4.
[17] Ayyanar R, Mohan N. Novel soft switching DC–DC converter with full ZVS-range and reduced filter requirement. I. Regulated-output applications. IEEE Transaction on Power Electronics 2001;16:184–92.
[18] Lee YS, Cheng GT. Quasi-resonant zero-current-switching bidirectional converter for battery equalization applications. IEEE Transaction on Power Electronics 2006;21:1213–24.
[19] Guidi G, Pavlovsky M, Kawamura A, Imakubo T, Sasaki Y. Improvement of light load efficiency of dual active bridge DC–DC converter by using dual leakage transformer and variable frequency. In: Proceedings of IEEE energy conversion congress and exposition (ECCE 2010); 12–16 September, 2010. p. 830–837.
[20] Li X, Bhat AKS. Analysis and design of high-frequency isolated dual-bridge series resonant DC/DC converter. IEEE Transactions on Power Electronics 2010;25:850–62.
[21] Song YJ. Analysis and design of high frequency link power conversion systems for fuel cell power conditioning. PhD thesis. TX: A&M University USA; 2004.
[22] Haihua Z, Khambadkone AM. Hybrid modulation for dual-active-bridge bidirectional converter with extended power range for ultracapacitor application. IEEE Transactions on Industry Applications 2009;45:1434–42.
[23] Krismer F,Round S, Kolar JW.. Performance optimization of a high current dual active bridge with a wide operating voltage range. In: Proceedings of the 37th IEEE power electronics specialists conference, PESC '06; 2006. p. 1–7.
[24] Lei W, Zhan W, Hui L.. Optimized energy storage system design for a fuel cell vehicle using a novel phase shift and duty cycle control. In: Proceedings of IEEE energy conversion congress and exposition (ECCE 2009). San Jose: USA; 20–24 September. 2009. p. 1432–1438.
[25] Oggier GG, Garcia GO, Oliva AR. Switching control strategy to minimize dual active bridge converter losses. IEEE Transactions on Power Electronics 2009;24:1826–38.
[26] Zhan W, Hui L.. Optimized operating mode of current-fed dual half bridges DC–DC converters for energy storage applications. In: Proceedings of IEEE energy conversion congress and exposition (ECCE 2009). San Jose: USA; 20–24 September, 2009. p. 731–737.
[27] Huafeng X, Shaojun X. A ZVS bidirectional DC–DC converter with phase-shift plus PWM control scheme. IEEE Transactions on Power Electronics 2008;23:813–23.
[28] Schibli N. DC–DC converters for two-quadrant operation with controlled output voltage, In: Proceedings of european conference on power electronics and applications (EPE), Lausanne; 1999. p. 1–7.
[29] Zhang Z., Ruan X.. A novel double phase-shift control scheme for full-bridge three-level converter. In: Proceedings of the applied power electronics conference (APEC). 2005; vol. 2: p. 1240–1245.
[30] Song Y, Enjeti PN. A new soft switching technique for bi-directional power flow, full-bridge DC–DC converter. In: Proceedings of 37th IEEE industry applications conference (IAS 2002); 2002. p. 2314–2319.
[31] Jain AK, Ayyanar R. PWM control of dual active bridge: comprehensive analysis and experimental verification. IEEE Transactions on Power Electronics 2011;26:1215–27.
[32] Haimin T, Kotsopoulos A, Duarte JL, Hendrix MAM. Transformer-coupled multiport ZVS bidirectional DC–DC converter with wide input range. IEEE Transactions on Power Electronics 2008;23:771–81.
[33] Zhang Z, Ouyang Z, Thomsen O, Andersen M. Analysis and design of a bidirectional isolated DC–DC converter for fuel cell and super-capacitor hybrid system. IEEE Transactions on Power Electronics 2012;27:848–59.
[34] Krismer F, Kolar JW. Accurate power loss model derivation of a high-current dual active bridge converter for an automotive application. IEEE Transactions on Industrial Electronics 2010;57:881–91.